

Photonic Active Bowtie Nanoassemblies with Chirality Continuum

Nicholas Kotov (✉ kotov@umich.edu)

University of Michigan <https://orcid.org/0000-0002-6864-5804>

Prashant Kumar

University of Michigan <https://orcid.org/0000-0003-4622-0917>

Thi Vo

University of Michigan

Minjeong Cha

UNIVERSITY OF MICHIGAN <https://orcid.org/0000-0001-8721-7111>

Anastasia Visheratina

University of Michigan, Ann Arbor

Ji-Young Kim

University of Michigan, Ann Arbor <https://orcid.org/0000-0001-5631-957X>

Wenqian Xu

Argonne National Laboratory

Jonathan Schwartz

University of Michigan, Ann Arbor

Alexander Simon

University of Michigan, Ann Arbor

Daniel Katz

University of Michigan, Ann Arbor

Emanuele Marino

University of Pennsylvania

Won Jin Choi

University of Michigan <https://orcid.org/0000-0001-6303-8899>

Si Chen

Argonne National Laboratory

Christopher Murray

University of Pennsylvania

Robert Hovden

University of Michigan <https://orcid.org/0000-0002-3403-8803>

Sharon Glotzer

University of Michigan–Ann Arbor <https://orcid.org/0000-0002-7197-0085>

Physical Sciences - Article

Keywords:

Posted Date: May 20th, 2022

DOI: <https://doi.org/10.21203/rs.3.rs-1614619/v1>

License:  This work is licensed under a Creative Commons Attribution 4.0 International License.

[Read Full License](#)

Version of Record: A version of this preprint was published at Nature on March 15th, 2023. See the published version at <https://doi.org/10.1038/s41586-023-05733-1>.

Abstract

Chirality is a geometrical property described by continuous mathematical functions.^{1–5} However, in chemical disciplines chirality is often treated as a binary left/right characteristic of molecules rather than a continuity of chiral shapes. While being theoretically possible, a family of stable chemical structures with the same shape and progressively tunable chirality is yet unknown. Here we present such structures in the form of nanostructured microparticles with anisotropic bowtie shape and widely tunable twist angle, pitch, size, thickness, and length. The self-limited assembly of the bowties enables high synthetic reproducibility, size monodispersity, and computational predictability of their geometries for different assembly conditions.⁶ The bowties nanoassemblies display multiple strong circular dichroism peaks originating from absorptive and scattering phenomena. Unlike classical chiral molecules, these particles display a continuum of chirality measures² that correlate exponentially with the spectral positions of the circular dichroism peaks. Bowtie particles with variable polarization rotation were used to print photonic active metasurfaces with spectrally tunable positive/negative polarization signatures for light detection and ranging (LIDAR) devices.

Full Text

Mathematical definitions of mirror asymmetry^{1–5} recognize the continuity of chiral geometries that can be visualized by gradual stretching of macroscale helical springs to obtain different periodicities of coils, referred to as pitch. At smaller scales, continuously variable chirality can be observed for origami/kirigami sheets,^{7–9} nanocomposites^{10,11} and some polymeric solids whose shape and circular dichroism can be varied by mechanical deformation and external fields.¹² However, chirality in chemistry commonly manifests as a binary property: chiral molecules are either right-handed or left-handed. Small chiral molecules are typically known as *D/L* or *R/S* enantiomers, while larger molecules with helical shapes are often denoted as Δ/Λ or *M/P* enantiomers. The binary chirality of, for instance, amino acids, originates from a high-energy penalty for distorting the optical center based on sp^3 -carbon atoms. The discreteness of chirality in liquid crystals,¹³ macromolecular compounds,¹⁴ helical polymers¹⁵ and nanoparticles (NPs)^{16,17} manifests in abrupt transitions between chiral phases with different crystallinity or particle shapes.¹⁸ Energy penalties are relaxed for large flexible molecules,¹⁹ supramolecular complexes,^{16,20,21} and biopolymers,^{18,22,23} but the restrictions on chiral shapes remain nevertheless stringent. Unlike macroscale springs, the helical pitch across the entire variety of biomolecules varies surprisingly little. For DNA as well as protein α -helices and β -sheets, pitch changes only in the range of 11 – 46 Å, 2.3 – 5.5 Å, and 7 – 8 Å, respectively; these narrow ranges are essential for precise folding of biomolecules.²⁴

The transition from discrete chiral phases and shapes to a palette of chemical compounds with widely and continuously tunable chirality would be transformative for the development of chiral photonics and chiral metamaterials – two rapidly developing fields – as well as for established fields of biochemical separations and chiral catalysis. Fundamentally, availability of continuously variable chiral compounds is

essential for establishing correlations between chirality measures and chemical properties. For instance, the attempts to correlate optical activity with a variety of chirality measures has largely failed, so far.^{25,26}

Here we show that continuously variable chiral geometries are possible for nanostructured microparticles with bowtie shapes. These particles are hierarchically assembled nanoribbons containing helical chains of cystine (CST, the dipeptide of cysteine bonded via S-S bridge) interconnected by Cd²⁺ ions. The finely controlled balance between short- and long-range interactions and defect tolerance of the assembly process enable the synthesis of bowties with widely tunable twist angle, pitch, size, thickness, and length.

Synthesis and structural characterization. To synthesize the bowties, we mixed an aqueous solution of Cd²⁺ with an aqueous solution of *L*- or *D*-cystine (CST) (**SI Fig. 1a,b**). For example, 10 μ l of (1 mM) CdCl₂ and 10 μ l of (1 mM) *L*-CST were added to 1 mL of water at room temperature and pH 11, which resulted in bowties with pitch (p), width (w), thickness (t), and length (l) of 4.1 μ m, 1.3 μ m, 0.5 μ m, 3.1 μ m, respectively (**Fig. 1a**). The synthesis of the bowtie particles is 100% enantioselective with *L*- and *D*-CST resulting in correspondingly left- and right-twisted bowties exclusively (**Fig. 1a,c, Video S2**). The resulting particles are uniform in shape, size, and handedness with standard deviation in p , w , t , and l of 19.0%, 13.6%, 11.9%, and 11.5%, respectively. Relative monodispersity of the bowtie particles indicates that they are formed in a self-limited assembly process (**SI Fig. 12**).^{5,6} Nanostructured microparticles resembling a stack of flat nanoscale ‘pancakes’ are observed when *rac*-CST is used (**Fig. 1b**).

Electron microscopy, X-ray diffraction (XRD), and electron diffraction reveal several levels of hierarchical organization within the cadmium cystinate bowties (**Fig. 1i, Fig. 2a**). Scanning electron microscopy (SEM) images for the terminal (**Fig. 1a-c**) and intermediate (**Fig. 2a,b**) stages of the synthesis show that the bowtie nanoassemblies are structured as a stack of twisted nanoribbons 200 – 1200 nm in length and 45 nm in thickness (**Video S1**). In turn, the nanoribbons are assembled from nanoplatelets 50 – 200 nm in length (**Fig. 2c,d**) and a thickness of \sim 1.2 nm calculated from the solved crystal structure. The judicial examination of the bowtie structural data (**SI Fig. 10**) indicates that the nanoplatelets are formed from nanoclusters 1-2 nm in size, which is consistent with the thickness of the nanoplatelets and previous studies of nanoassemblies.²⁷ The nanoribbons and bowties acquire progressively stronger twist as the enantiomeric excess ($\pm\chi$) of *L*- or *D*-CST increases (**Fig. 2f**).

To understand better how the atomic structure of the bowtie nanoassemblies can accommodate their continuous changes in chirality while remaining chemically stable, we show synchrotron XRD patterns for particles in **Figs. 1a-c**. Solving for the atomic structure followed by Rietveld refinement suggested several polymorphs of *L*-CST coordinated with Cd atoms (**SI Fig. 5-8, SI Table 1**), indicating the possibility of variable atomic organization. Cumulative analysis of the XRD models points to Cd₂CST₂ nanoclusters (**Fig. 1j**) as the elementary structural unit of the nanoribbons (**SI Fig. 8**). These units contain helical chains (**Fig. 1j,k, SI Fig. 8**) enabling partial swapping of *L*-CST for *D*-CST without drastic disruption of the short-range coordination bonds. The amine and carboxylic groups located on the exterior of the helical chains can form hydrogen bonds with neighboring ones stabilizing the structure and facilitating the

nanosheet stacking (**Figs. 1j,k, 2c-d**). Importantly, XRD data indicate that the atomic organization in the nanosheets is imperfect, as evidenced by peak overlap below 2.5 Å. This imperfection is necessary for the chemical structure to produce the multiplicity of twisted shapes.

Selected area electron diffraction (SAED) from a single nanoribbon confirms the structural analysis based on XRD (**Fig. 2e**). Cryo-SAED patterns show characteristic reflections at 4.9 Å, 4.6 Å, and 4.1 Å, which are consistent with corresponding distances between planes in the orthorhombic Cd₂CST₂ structure at 5.1 Å, 4.5 Å, and 4.1 Å (**SI Fig. 9**). The nanoribbons are polycrystalline, revealing fairly ordered domains of helical chains as observed from sharp spots in the SAED pattern (**Fig 2e, SI Fig. 15**). Some degree of polycrystallinity enables the nanoribbons to accommodate CST ligands of opposite chirality while retaining the physical integrity of the nanoassembly.

The flexible hydrogen-bonded networks between the nanoribbons can accommodate variable bond angles^{17,18}, which is one of the factors enabling variable chirality. The ability of all nanoscale building blocks from cadmium cysteinate to ionize, as evidenced by the high zeta-potential (**Fig. 1g,h**), is also significant. The surface potential of the nanoscale particles and resulting long-range repulsive interparticle interactions can be varied over a wide range by tuning pH and ionic strength, enabling controlled variability of the bowtie geometries. The twist of the nanoribbons makes the electrostatic interactions chiral, which reinforces the handedness of their stacking and therefore the similarity of the particle shapes. Other contributing interactions include mechanical deformations of the nanoribbons that accommodate the atomic and nanoscale preferences of the two-dimensional assemblies.^{17,28,29}

Multispectral photonic activity. Extinction and circular dichroism (CD) spectroscopies from ultraviolet to terahertz (THz) frequencies demonstrate that the left- and right-handed bowties display a rich set of mirror symmetric bands, while the 'pancake stack' assemblies are chiroptically silent (**Fig. 1d,f**). Visible, Raman, FTIR, mid-IR, and THz spectra (**Figs. 1d-f**) confirm the molecular structure of the bowtie nanoassemblies established by XRD and SAED. Raman spectra (**SI Fig 2a**) show characteristic peaks at 510 cm⁻¹ corresponding to S-S disulfide stretches. The strong and wide band from 3000 to 3750 cm⁻¹ observed in FTIR spectra confirms the multiplicity of hydrogen bonds involved in stabilization of the nanoribbons and their stacks. The UV CD spectra have multiple positive and negative peaks denoted as P1 (-, 1040 nm), P2 (+, 460 nm), P3 (-, 330 nm), P4 (+, 270 nm), and P5 (-, 235 nm), from the longest to the shortest (**Fig. 1f**). Among them P5 and P4 in the UV part of the spectrum are attributed to electronic transitions in the CST ligands. These two peaks are broadened and red-shifted compared to free CST due to coordination with Cd²⁺ and exchange interactions with other states. VCD spectra are approximately 100 times stronger than those of free CST due to long-range resonant coupling between helical chains forming cadmium cysteinate nanoribbons. The VCD band near 1600 cm⁻¹ (**Fig. 1e**) is typically a simple bisignate peak for free CST, but it is split into five bands in the bowtie particles due to the asymmetric environment around the nitrogen and oxygen atom involved in coordination bonding with the cadmium atom when forming the bowties (**Fig. 1j,k, SI Fig. 6**). THz circular dichroism shows the existence of chiral phonons propagating along the nanoribbons (**Fig. 1d**).³⁰ Besides substantiating the

hierarchical organization of the bowties, these data firmly indicate that the bowties made with *L*- or *D*-CST are true multiscale enantiomers for which the mirror asymmetry is present at all molecular, sub-nanometer, nanometer, and micrometer scales.

Modeling of bowtie assembly. Computational models of bowtie formation reveal the process of hierarchical self-assembly essential for their morphological uniformity, high yield, and tunable chirality. Based on XRD, transmission electron microscopy (TEM), and spectroscopic data, we constructed a coarse-grained version of the basic nanocluster with helical chains (SI Fig. 11) as the building block for nanoribbons and nanosheets (see Methods). A Monte Carlo (MC) growth algorithm was then employed to simulate bowtie assembly. Based on zeta potential measurements (Fig. 1g,h, SI Fig. 17,18), we defined an average net charge on each nanocluster to be +1. Because the addition of each new nanocluster increases the total charge of the growing particle, the self-assembly process is electrostatically restricted,³¹ with each additional nanocluster having to overcome an increasingly repulsive energy barrier. Computation of the pair-wise potentials (Fig. 2g,h) between nanoclusters for *L*-monochiral and racemic versions of the nanoclusters, abbreviated as LCL or LCD, respectively, revealed growth directions along which the nanoclusters interact through hydrogen bonding between –COOH and –NH₂ groups. These growth directions reflect the hierarchy of structural formation observed in experiments: that is, nanoclusters assemble into nanoplatelets, that grow into nanoribbons due to geometrical anisotropy of attractive potentials. In turn, the nanoribbons stack to form the observed bowtie hierarchical nanoassemblies. As the number of building blocks in the assembly increase, the size of the ordered domains in the nanoribbons also increases (shown by color in Fig. 2i, SI Fig. 13). The growth of nanoribbons stops when the net charge repulsion on the particle becomes strong enough to prevent further attachment of nanoclusters (SI Fig. 32), balancing out the attractive forces arising from short-range coordination bonds, hydrogen bonding, and vdW interactions. LCL nanoclusters form a twisted platelet (Fig. 2j, top row), while LCD nanoclusters form a flat sheet (Fig. 2j, bottom row). Remarkably, the model predicts correctly that the enantiomeric composition of the nanoclusters, χ , determines the chirality of the bowtie microparticles propagating up in scale as the particles evolve in size. The high efficacy of such multiscale chirality transfer for different χ results in the bowties' uniform pitch and size (Fig. 2f, SI Fig. 29).

Tunable interparticle forces lead to tunable chirality. Electrostatically restricted, hierarchical assembly from chiral nanoclusters enables wide-range tuning of electrostatic repulsion, van der Waals forces, hydrogen bonding, and other interactions by changing temperature, solvent, salt concentration, counterions, etc. (SI Fig. 21). Among the multiplicity of permutations of assembly parameters, it is instructive to consider three cases that together exemplify the ways in which different interparticle interactions can be used to 'tune' the bowtie geometry. *Case 1:* The increase of ionic strength results in the increase of l , w , and t because the range of electrostatic interactions is reduced for high ionic strengths (SI Fig. 16). *Case 2:* The increase of the zeta-potential with pH results in the increase of l , w , and t . De-protonation of the –COOH groups on the surface of nanoribbons and nanoplatelets results in the concomitant reduction of the hydrogen bonding between the ribbons in the stack and, thus, in the greater separation between the

nanoribbons (**SI Figs. 17,18**). *Case 3*: An increase of *L*-CST/Cd ratio leads to the increase of *l*, *w*, and *t* due to adsorption of the counter-ions on the bowtie surface (**SI Fig. 14a**). The increase of the CST concentration simultaneously promotes (**Fig. 3a, SI Fig. 16,22**) the close-range hydrogen bonding between the nanoclusters, resulting in thicker and wider nanoribbons (**Fig. 3a; SI Fig. 20**).

The variability of the twist angle and pitch serves as a vivid demonstration of the tunable chirality of these particles (**SI Fig. 29**). The computational model describing the hierarchical self-assembly of the bowties from nanoclusters with intermediate formation of nanoplatelets and nanoribbons, quantitatively predicts their geometry (**SI Fig. 27,20,31**). It also correctly captures the variations of the geometrical parameters of the bowtie nanoassemblies in response to variations of ionic screening, solvents, enantiomeric excess, temperature, and counter-ions (**Fig. 3d,e, SI Fig. 21-29, Fig. 33-37**).

The chirality continuum of the bowtie particles can be demonstrated by calculating chirality measures such as the Hausdorff chirality measure,¹ the continuous symmetry measure,² or the Osipov–Pickup–Dunmur (OPD) chirality measure (See SI).³ While all of these measures are suitable for establishing the variable chirality of the bowties, the OPD has additional feature - it changes the sign when switching from left to right enantiomers. The transition from discrete to continuous chirality is evident from **Figs. 3d,e** because the pitch and OPD cover a wide range of values. For example, the OPD varies gradually from -4.7 to +4.6, while other molecular or nanoscale systems have only discrete points. Testing the correlation between the sign of the peaks in the circular dichroism spectra (**Fig. 2f, 4a, SI Fig. 41**) is fundamentally important because of the long-standing controversy about suitability of sign-changing pseudoscalar measures of chirality for description of experimental data.^{5,32} We found that the sign of OPD correlates well with the experimental mirror symmetry of the CD and *g*-factor spectra as well as the signs of P3, P2, and P1 peaks (**Fig. 4a, SI Fig 41**).^{5,32} Quite unexpectedly, we also observed an exponential relationship between OPD and the spectral position of the P2 and P3 peaks (**Fig. 4c**). We note that organic and biological chemistries do not provide, hitherto, examples of quantifiable property–chirality relationships, despite extensive discussions of their possibility.^{4,5,25,33}

Bowtie-based photonic materials and surfaces. In addition to the continuity of chiral shapes, the experimentally observed dependences of spectral characteristics of P2/P3 peaks versus OPD indicate that the physical laws governing chirality-property relationships for nanostructured microparticles and small molecules are different, which necessitated us to seek a deeper understanding of light-matter interactions in bowties. Such knowledge may also facilitate the design of photonic materials in the visible and near-infrared (NIR) parts of the spectrum.

We found that the computational models describing bowties as single twisted ribbons accurately explain the red shift and all other spectral trends of P3, P2, and P1 peaks across the entire parameter space (**Fig 4a,d,e SI Fig. 21, 23, 24, 33-37, 39**). Taking left-handed models corresponding to bowties made from *D*-CST as an example, decomposition of the extinction spectra into scattering and absorptive components revealed that the positive P3 and P1 peaks in **Fig. 1f** and mirror symmetric negative P3 and P1 (for right-handed bowties) in **Fig.4a** are from differential scattering. The computational predictions for

peak position match experiments nearly perfectly (**Figs.3a,b, SI Fig.22,23,39,42-44**). Analysis of electrical and magnetic field distributions indicates that P1 and P3 originate from the dipolar and quadrupolar resonance scattering modes, respectively (**Fig 4f, SI Figs. 45,47, Video S3-S4**). We also found that the P2 peak (negative for left-handed bowties) corresponds to the absorption of circularly polarized photons (**SI Fig. 46**) for all chiral particles studied here. Although the peak positions vary with particle size, the attribution of the peaks remains the same for all l , w , t , and θ , as can be demonstrated by the calculations for the different models (**SI Fig. 44**). Note that both scattering and absorption peaks of bowties involve the interaction of photons with the particle as a whole, not specific quantum states, which is essential for understanding the origin of observed chirality-property relationships (**Fig 4a-d**). Optical properties of small molecules originate from chiral shapes of molecular orbitals that may or may not correlate with the geometry of the sp^3 carbon atom or Δ/Λ enantiomers. Therefore, the similarity of the physical dimensions of chiral objects in bowties and incident photons engenders the observed dependences (**Fig.4c**) and, thus, the vast differences in chirality-property relationships in comparison with small molecules, polymers and other typical chemical species, bringing them closer to the photonic metamaterials.⁷⁻¹¹

Detailed understanding of the optical nature of the observed polarization peaks along with the simplicity of bowtie synthesis and the predictive relationship between particle structure and optical properties opens the door to the engineering of particle-based metasurfaces. Coatings with distinct circular polarization signatures (**SI Fig. 49**) are needed for example, for machine vision systems to increase the accuracy of object identification (e.g. pedestrians). As a demonstration, we synthesized bowtie particles with strong circularly polarized P1 peak scattering in the NIR part of the spectrum. They were dispersed in water and then mixed with poly-acrylic acid (PAA). These dispersions were printed on glass slides and cotton fabric. A LIDAR operating at 1550 nm with circularly polarized beam (**SI Fig. 48**) was utilized to acquire images of the printed objects following their decomposition into left- and right-handed components of back-scattered light originating from the dipolar P1 peak in CD spectra (**Fig. 1f**). The distinct contrast between prints made from the left- and right-handed bowties was observed (**Fig. 4g, SI Fig 49, 50**). The layer of left-handed bowties can also be identified with high contrast on cotton cloth in LIDAR images (**SI Fig. 49d,e**), which can be utilized in autonomous vehicles and other robots for the identification of pedestrians. The polarization contrast originates from the micron-scale chirality of the fabric itself that can also be continuously tuned.

Conclusions

Hierarchical stacking of electrostatically charged twisted nanoribbons creates flexible assembly patterns producing a large family of nanoassemblies with widely variable bowtie geometries. Conversion of Cd-CST bowties into similarly shaped CdS particles indicates that multiple other materials can be prepared with the same diversity of geometries and dimensions (**SI Fig. 9**). Strong mirror symmetric dipolar and quadrupolar photonic resonances for light scattering and absorption create a rich and tunable set of polarization rotation peaks across the technologically relevant visible and infrared parts of the

electromagnetic spectrum, which enables chirality-based engineering of microparticles and composite materials for robotic, automotive, chemical and biomedical technologies. Facile dispersion of the bowtie particles in water translates into the emerging opportunity of printable metasurfaces, which can simplify their scalable manufacturing and utilization.

Methods

Synthesis of bowties. Cadmium chloride (CdCl_2), 99.99% trace metals basis, *L*-CST, $\geq 98\%$ (TLC), crystalline, *D*-CST, 98%, sodium hydroxide (NaOH) pellets $>97\%$ were purchased from Sigma-Aldrich. De-ionized water (18.2-m Ω -cm) was used for the preparation of stock solutions and aqueous dispersions. 10 mL stock solutions of CdCl_2 (0.1 M), *L*-CST (0.1 M), *D*-CST (0.1 M) and NaOH (2.5 M) were prepared by dissolving the required amounts in DI water. pH of CST stock solution was raised to 11 by adding 1 mL of 2.5 NaOH in 10 ml of solution. An immediate change in appearance was observed by the formation of a clear solution. Remaining solids were dissolved by mild-sonication for 10 seconds. Bowties were synthesized by the mixing stock solutions of CdCl_2 and *L*-CST or *D*-CST in 1:1 stoichiometric ratio in an aqueous media. Typical synthesis involved 20 μL of *L*-CST added to 960 μL of water followed by the addition of 20 μL CdCl_2 . The solution mixture was shaken vigorously until the dispersion turned milky, which is an indicator of the bowties assembly process. After that, the mixture was kept still at room temperature for 15 minutes to ensure the completion of the self-assembly. The dispersion was subsequently centrifuged three times in DI water at 6000 rpm for 3 mins. Final aqueous dispersion was stored at room temperature and used for further characterization and studies.

Electron microscopy. Scanning electron microscopy (SEM) samples were prepared by drop-casting 5 μL of aqueous dispersion on 1 cm \times 1 cm silicon wafers (TedPella), following by drying at room temperature. This was followed by sputter coating a 5-10 nm film of gold on the wafer to avoid charging due to the electron beam. SEM measurements were performed in FEI Nova NanoLab Dual Beam SEM and FEI Helios Nanolab at 5 kV accelerating voltage and 0.4 nA beam current under secondary electron detection mode.

TEM samples were prepared by drop-casting 10 μL of aqueous solution on to a copper grid coated with holey carbon supported by a continuous carbon film (TedPella 01824). Bright-field TEM was performed on JEOL 2010 operating at 300 kV accelerating voltage and acquisition were done using Gatan OneView camera. ADF-STEM and STEM-EDX measurements were performed on cold-FEG JEOL 3100R05 with Cs aberration correction operating at 300 keV. A HAADF detector was to acquire Z-contrast images where the intensity is proportional to the atomic number of the column over which the electron probe is placed. Diffraction experiments were acquired using Thermo Fisher Talos F200X operated at 200keV equipped with a Gatan One View camera. The Elsa (698) Gatan Cryo Holder cooled specimens down to ~ 93 K for low-temperature measurements.

STEM Tomography. The synthesized bowtie particles were dispersed in water and drop cast using a micropipet onto a 3 mm copper TEM grid dried at room temperature. The TEM grid was an ultrathin (3 nm) carbon film with a large hexagonal mesh (100) to provide high specimen tilts without beam

shadowing (Electron Microscopy Sciences, Hatfield, PA, USA). The tomographic tilt series were acquired using a Thermo Fisher Talos F200X operated at 200 keV as a scanning transmission electron microscope with a 10.5 mrad semi-convergence angle using a 36 mrad and 165 mrad inner and outer semi-collection angles for the annular dark field (ADF) detector. The right-handed bowtie particles was acquired over a tilt range of -72° to $+73^\circ$ and left-handed bowtie particles specimen was acquired over a tilt range of -75° to $+71^\circ$ both with a $+1^\circ$ tilt increment. At each angle, annular dark-field images of size 1024×1024 pixels were recorded with a dwell time of $4 \mu\text{s}$ and pixel size of 4.94 nm. The tomograms were reconstructed with the additive simultaneous iterative reconstruction technique for 150 iterations. The three-dimensional reconstructions were visualized by *tomviz*³⁴

X-Ray Diffraction. Synchrotron X-ray powder diffraction data ($\lambda = 0.45192 \text{ \AA}$) was collected at Beamline 17-BM at the Advanced Photon Source at the Argonne National lab. Freeze dried powder sample of L-/D-/rac-bowties was loaded in a 1.0 mm diameter Kapton capillary tube, which was then measured using a VAREX XRD 4343CT amorphous silicon area detector in the Debye-Scherrer geometry.

Measurements of particle geometry. Length (l), width (w), thickness (h) and angle of twist (θ) as defined in **Fig. 3c** were measured using Jann5s/measure tool from Matlab central. A minimum of 10 measurements was done for each parameter and standard deviation (σ) was calculated and represented

as percentage variation by following equation
$$\text{error} = \frac{\sigma_x}{x} \times 100,$$
 where $x = l, w, h, \theta$ and $\frac{x}{x}$ is the mean of corresponding values.

Finite-difference time-domain (FDTD) simulations of optical properties. The CD and g-factor spectra were calculated using a commercial FDTD software package (Lumerical Solutions Inc.; www.lumerical.com/tcad-products/fdtd/). We used total-field scattered-field (TFSF) sources that surrounded the structure being modeled. CPL was generated by positioning two TFSF sources along the same forward axis at a 90° angle and with a phase difference of either -90° for photons with left-handed polarization (LCP) or 90° for photons with right-handed polarization (RCP). Two analysis groups using box power monitors monitored the absorption and scattering cross sections (extinction is the sum of absorption and scattering). The FDTD simulation region was defined by a larger box monitor with a stretched-coordinate perfectly matched layer and non-uniform mesh type. Frequency profile monitors were inserted in the total field region to calculate electric field distribution in 3D. The refractive index for water is 1.33. Convergence tests with different mesh sizes were performed to determine the best balance between computational time restraints and simulation accuracy. Simulations were carried out for the bowties orientated with their long axis being parallel with the propagation direction (k -vector) of photons. 10-nm and 1 nm mesh size produced similar CD spectra; therefore, we used 10-nm mesh size for bowtie simulations presented in **SI Figs. 43-46**.

Chiroptical spectroscopy. Circular dichroism measurements in UV-vis and NIR range were performed using JASCO J-1700 equipped with one PMT detector in 200-800 nm range and two InGaAs NIR detectors in 800-1600 nm range. Typical scanning parameters were as follows: scanning speed, 500 nm/min; data

pitch, 0.1 nm; bandwidth, 5 nm (NIR bandwidth, 10 nm), digital integration time, 0.25 s; and one accumulation. The anisotropy g -factor was calculated according to the equation $g = \frac{CD}{32,980 \times abs}$, where CD is the signal obtained from CD/DC channel, abs is the absorbance calculated from ABS and DC channels of the spectrophotometer. CD spectra were stopped at wavelengths where the HT voltage was greater than 800 V to avoid artifacts during acquisition.

Terahertz circular dichroism spectroscopy (TCD). Terahertz (THz) time-domain polarimetry system based on a three linear polarizers was used to measure absorption coefficients and THz circular dichroism spectra.⁷ We used calculations of Stokes parameters based on the E_x and E_y , the electric field in x and y directions, respectively. Absorption coefficients were extracted from the equations used in ref.⁷ after retrieval of phase from the transmission data. To eliminate linear birefringence effects from samples, highly concentrated mixture of bowtie powders with mineral oil was used. The reference sample is a quartz sandwich cell filled with mineral oil.

Vibrational circular dichroism spectroscopy. VCD measurements were performed on freeze-dried bowtie samples dispersed in heavy water (D_2O) at 33 mg/ml concentration. A 100 μ l drop was sandwiched between two BaF_2 crystals separated by a 50 μ m Teflon spacer. An MCT-V detector was used to acquire IR and VCD data in the range 2000 to 850 cm^{-1} with a resolution of 4 cm^{-1} and a total of 100 and 500 accumulations respectively. The sandwiched dispersion between BaF_2 crystals was rotated along a axis coinciding with the direction of the beam at a constant speed to avoid settling of particles. Corresponding IR and VCD were plotted as A and ΔA respectively with exclusion of the 1300 to 1100 cm^{-1} range that corresponds to strong absorption from D_2O .

Coarse-Grained Modeling of Bowtie. We pick features consistent with XRD results to construct a coarse-grained building block for the nanoclusters. The key features we chose to adapt are (**SI Fig. 11**): 1). Flat, rectangular prism-like building blocks with rough dimensions of 20 x 10 x 5 commensurate with XRD nanoclusters. 2). H-bonding sites decorate the two largest and two smallest facets to reflect the bonding between the $-COOH$ and $-NH_2$ groups. 3). The two intermediate facets exhibit directional interaction to capture the disulfide bridge formation intrinsic to CST. These interactions sites only interact with themselves. 4). Building block exhibit a slight shear on one facet to enforce chirality of L -CST vs R -CST. 5). Isotropic charge-charge repulsion between Cd^{2+} atoms embedded inside the building block – each has a net charge of +1 to build in charge-driven, self-limiting behaviors. 6). All other surface sites not defined above exhibit steric repulsion.

Potential of Mean Force and Monte Carlo Growth Simulation. Potential of mean force (PMF) between nanoclusters are computed by summing together all interactions as a function of the center-to-center distance between nanocluster pairs and performing weighted averaging. The resulting PMFs between L -CSTs (LCL) highlight directional growth features that are commensurate with the hierarchy of structural formation observed in experiments (**Fig. 2g**). PMFs computed for a mix of L -CST and R -CST (LCD)

conversely suggest a reduction in hierarchical structural formation and chiral propagation (**Fig. 2h**). We then employ the computed PMFs to perform Monte Carlo growth simulations. Specifically, the well depth of each computed PMF plus the net charge-charge repulsion between the next nanocluster and growing structure are employed as the input energy in the Metropolis algorithm. This enables Boltzmann weighted selection of the direction with which to place the next building block in the growing structure. Visualization of the growth simulation results confirm the formation of bowtie and pancake morphologies (**Fig. 2i,j**).

Declarations

Acknowledgements. Supported by the Vannevar Bush DoD Fellowship to N.A.K. titled “Engineered Chiral Ceramics” ONR N000141812876, NSF project “Energy- and Cost-Efficient Manufacturing Employing Nanoparticles” (NSF 1463474, ONR N000141812876); NSF 1566460 “Nanospiked Particles for Photocatalysis”; NSF grant 1538180; NSF grant DMR-9871177 for funding the JEOL 2010F analytical electron microscope used in this work. Support for the Dual Source and Environmental X-ray Scattering Facility at the University of Pennsylvania was provided by the Laboratory for Structure and Matter, which is funded in part by NSF MRSEC 1720530. T.V, S.C.G, E.M., C.B.M and N.A.K. were supported by Office of Naval Research Multidisciplinary University Research Initiative Award ONR N00014-18-1-2497; an MEC/PET fellowship (2014–2020). R.H. acknowledges support from ARO grant no. W911NF- 22-1-0056.

Contributions

P.K. and N.A.K. designed the project. P.K. conducted the synthesis of libraries of bowties with assistance from A.S. and D.K. P.K. measured VCD, CD data. W.J.C. measured the TCD data. P.K., W.Q, S.C., acquired, solved and refined the crystal structure from XRD data with input from N.A.K. P.K. conducted all the SEM imaging. J.S, P.K. and R.H. conducted the TEM and tomography measurements. T.V. and S.C.G. conducted the monte-carlo growth simulations and theoretical model development for structure prediction with input from P.K. and N.A.K. J.Y.K, A.V. and P.K. calculated the OPD indices from SEM images. P.K. simulated the chiroptical properties with input from N.A.K. E.M. and C.B.M. measured single particle scattering data. M.C. and N.A.K. conducted the LIDAR measurement and analysis. All the authors discussed the results. P.K. and N.A.K. wrote the manuscript with written contributions from all the authors. N.A.K directed all aspects of this project.

Conflicts of Interests: No conflicts of interest are reported. N.A.K is a founder of a start-up company Photon Semantics developing LIDAR technologies for machine vision.

References

- (1) Buda, A. B.; Mislow, K. A Hausdorff Chirality Measure. *J. Am. Chem. Soc.* **1992**, *114* (15), 6006–6012. <https://doi.org/10.1021/ja00041a016>.

- (2) Osipov, M. A.; Pickup, B. T.; Dunmur, D. A. A New Twist to Molecular Chirality: Intrinsic Chirality Indices. *Molec. Phys.* **1995**, *84* (August), 1193–1206. <https://doi.org/10.1080/00268979500100831>.
- (3) Zabrodsky, H.; Avnir, D. Continuous Symmetry Measures. 4. Chirality. *J. Am. Chem. Soc.* **1995**, *117* (1), 462–473. <https://doi.org/10.1021/ja00106a053>.
- (4) Rassat, A.; Fowler, P. W. Is There a “Most Chiral Tetrahedron”? *Chem. - A Eur. J.* **2004**, *10* (24), 6575–6580. <https://doi.org/10.1002/chem.200400869>.
- (5) Harris, A. B.; Kamien, R. D.; Lubensky, T. C. Molecular Chirality and Chiral Parameters. *Rev. Mod. Phys.* **1999**, *71* (5), 1745–1757. <https://doi.org/10.1103/RevModPhys.71.1745>.
- (6) Xia, Y.; Nguyen, T. D. T. D.; Yang, M.; Lee, B.; Santos, A.; Podsiadlo, P.; Tang, Z.; Glotzer, S. C.; Kotov, N. A. Self-Assembly of Self-Limiting Monodisperse Supraparticles from Polydisperse Nanoparticles. *Nat. Nanotechnol.* **2011**, *6* (9), 580–587. <https://doi.org/10.1038/nnano.2011.121>.
- (7) Choi, W.; Cheng, G.; Huang, Z.; Zhang, S.; Norris, T.; Kotov, N. A. Chiroptical Kirigami Modulators for Terahertz Circular Dichroism Spectroscopy of Biomaterials. *Nat. Mater.* **2019**, *18*, 820–826.
- (8) Nguyen, M.-K.; Kuzyk, A. Reconfigurable Chiral Plasmonics beyond Single Chiral Centers. *ACS Nano* **2019**, *13* (12), 13615–13619. <https://doi.org/10.1021/acsnano.9b09179>.
- (9) Dey, S.; Fan, C.; Gothelf, K. V.; Li, J.; Lin, C.; Liu, L.; Liu, N.; Nijenhuis, M. A. D.; Saccà, B.; Simmel, F. C.; Yan, H.; Zhan, P. DNA Origami. *Nat. Rev. Methods Prim.* **2021**, *1* (1), 13. <https://doi.org/10.1038/s43586-020-00009-8>.
- (10) Probst, P. T.; Mayer, M.; Gupta, V.; Steiner, A. M.; Zhou, Z.; Auernhammer, G. K.; König, T. A. F.; Fery, A. Mechano-Tunable Chiral Metasurfaces via Colloidal Assembly. *Nat. Mater.* **2021**, *20*, 1024–1028.
- (11) Kim, Y.; Yeom, B.; Arteaga, O.; Yoo, S. J.; Lee, S.-G.; Kim, J.-G.; Kotov, N. A. Reconfigurable Chiroptical Nanocomposites with Chirality Transfer from the Macro- to the Nanoscale. *Nat. Mater.* **2016**, *15* (4). <https://doi.org/10.1038/nmat4525>.
- (12) Miyajima, D.; Tashiro, K.; Araoka, F.; Takezoe, H.; Kim, J.; Kato, K.; Takata, M.; Aida, T. Liquid Crystalline Corannulene Responsive to Electric Field. *J. Am. Chem. Soc.* **2009**, *131* (1), 44–45. <https://doi.org/10.1021/ja808396b>.
- (13) Ohta, E.; Sato, H.; Ando, S.; Kosaka, A.; Fukushima, T.; Hashizume, D.; Yamasaki, M.; Hasegawa, K.; Muraoka, A.; Ushiyama, H.; Yamashita, K.; Aida, T. Redox-Responsive Molecular Helices with Highly Condensed π -Clouds. *Nat. Chem.* **2011**, *3* (1), 68–73. <https://doi.org/10.1038/nchem.900>.
- (14) Ma, W.; Kuang, H.; Wang, L.; Xu, L.; Chang, W.-S.; Zhang, H.; Sun, M.; Zhu, Y.; Zhao, Y.; Liu, L.; Xu, C.; Link, S.; Kotov, N. A. Chiral Plasmonics of Self-Assembled Nanorod Dimers. *Sci. Rep.* **2013**, *3*, 1934. <https://doi.org/10.1038/srep01934>.

- (15) Yashima, E.; Ousaka, N.; Taura, D.; Shimomura, K.; Ikai, T.; Maeda, K. Supramolecular Helical Systems: Helical Assemblies of Small Molecules, Foldamers, and Polymers with Chiral Amplification and Their Functions. *Chem. Rev.* **2016**, *116* (22), 13752–13990. <https://doi.org/10.1021/acs.chemrev.6b00354>.
- (16) Lee, H. E.; Ahn, H. Y.; Mun, J.; Lee, Y. Y.; Kim, M.; Cho, N. H.; Chang, K.; Kim, W. S.; Rho, J.; Nam, K. T. Amino-Acid- and Peptide-Directed Synthesis of Chiral Plasmonic Gold Nanoparticles. *Nature* **2018**, *556* (7701), 360–364. <https://doi.org/10.1038/s41586-018-0034-1>.
- (17) Jiang, W.; Qu, Z.; Kumar, P.; Vecchio, D.; Wang, Y.; Ma, Y.; Bahng, J. H.; Bernardino, K.; Gomes, W. R.; Colombari, F. M.; Lozada-Blanco, A.; Veksler, M.; Marino, E.; Simon, A.; Murray, C.; Muniz, S. R.; Moura, A. F. de; Kotov, N. A. Emergence of Complexity in Hierarchically Organized Chiral Particles. *Science* (80-.). **2020**, *368* (6491), 642–648. <https://doi.org/DOL: 10.1126/science.aaz7949>.
- (18) Medina, D. D.; Mastai, Y. Chiral Polymers and Polymeric Particles for Enantioselective Crystallization. *Isr. J. Chem.* **2018**, *58* (12), 1330–1337. <https://doi.org/https://doi.org/10.1002/ijch.201800174>.
- (19) Gingras, M. One Hundred Years of Helicene Chemistry. Part 3: Applications and Properties of Carbohelicenes. *Chem. Soc. Rev.* **2013**, *42* (3), 1051–1095. <https://doi.org/10.1039/C2CS35134J>.
- (20) Ma, W.; Xu, L.; de Moura, A. F.; Wu, X.; Kuang, H.; Xu, C.; Kotov, N. A. Chiral Inorganic Nanostructures. *Chem. Rev.* **2017**, *117* (12), 8041–8093. <https://doi.org/10.1021/acs.chemrev.6b00755>.
- (21) Aida, T.; Meijer, E. W.; Stupp, S. I. Functional Supramolecular Polymers. *Science* (80-.). **2012**, *335* (6070), 813–817.
- (22) Ho, R.-M.; Chiang, Y.-W.; Chen, C.-K.; Wang, H.-W.; Hasegawa, H.; Akasaka, S.; Thomas, E. L.; Burger, C.; Hsiao, B. S. Block Copolymers with a Twist. *J. Am. Chem. Soc.* **2009**, *131* (51), 18533–18542. <https://doi.org/10.1021/ja9083804>.
- (23) Wang, H.-F.; Yang, K.-C.; Hsu, W.-C.; Lee, J.-Y.; Hsu, J.-T.; Grason, G. M.; Thomas, E. L.; Tsai, J.-C.; Ho, R.-M. Generalizing the Effects of Chirality on Block Copolymer Assembly. *Proc. Natl. Acad. Sci.* **2019**, *116* (10), 4080 LP – 4089. <https://doi.org/10.1073/pnas.1812356116>.
- (24) Ido, S.; Kimura, K.; Oyabu, N.; Kobayashi, K.; Tsukada, M.; Matsushige, K.; Yamada, H. Beyond the Helix Pitch: Direct Visualization of Native DNA in Aqueous Solution. *ACS Nano* **2013**, *7* (2), 1817–1822. <https://doi.org/10.1021/nn400071n>.
- (25) Petitjean, M. Chirality and Symmetry Measures: A Transdisciplinary Review. *Entropy*. Molecular Diversity Preservation International July 3, 2003, pp 271–312. <https://doi.org/10.3390/e5030271>.
- (26) Buda, A. B.; der Heyde, T. A.; Mislow, K. On Quantifying Chirality. *Angew. Chemie Int. Ed. English* **1992**, *31* (8), 989–1007. <https://doi.org/10.1002/anie.199209891>.

- (27) Tang, Z.; Zhang, Z.; Wang, Y.; Glotzer, S. C.; Kotov, N. A. Self-Assembly of CdTe Nanocrystals into Free-Floating Sheets. *Science (80-)*. **2006**, *314* (5797), 274–278. <https://doi.org/10.1126/science.1128045>.
- (28) Gao, C.; Kewalramani, S.; Valencia, D. M.; Li, H.; McCourt, J. M.; Olvera de la Cruz, M.; Bedzyk, M. J. Electrostatic Shape Control of a Charged Molecular Membrane from Ribbon to Scroll. *Proc. Natl. Acad. Sci.* **2019**, *116* (44), 22030–22036. <https://doi.org/10.1073/pnas.1913632116>.
- (29) M., M. J.; Chaitanya, J.; Perna, S.; Arvind, B.; Aparna, B.; M., G. G.; F., H. M.; Zvonimir, D. Conformational Switching of Chiral Colloidal Rafts Regulates Raft–Raft Attractions and Repulsions. *Proc. Natl. Acad. Sci.* **2019**, *116* (32), 15792–15801. <https://doi.org/10.1073/pnas.1900615116>.
- (30) Choi, W. J.; Yano, K.; Cha, M.; Colombari, F. M.; Kim, J.-Y.; Wang, Y.; Lee, S. H.; Sun, K.; Kruger, J. M.; de Moura, A. F.; Kotov, N. A. Chiral Phonons in Microcrystals and Nanofibrils of Biomolecules. *Nat. Photonics* **2022**. <https://doi.org/10.1038/s41566-022-00969-1>.
- (31) Nguyen, T. D.; Schultz, B. A.; Kotov, N. A.; Glotzer, S. C. Generic, Phenomenological, on-the-Fly Renormalized Repulsion Model for Self-Limited Organization of Terminal Supraparticle Assemblies. *Proc. Natl. Acad. Sci. U. S. A.* **2015**, *112* (25). <https://doi.org/10.1073/pnas.1509239112>.
- (32) Millar, G.; Weinberg, N.; Mislow, K. On the Osipov–Pickup–Dunmur Chirality Index: Why Pseudoscalar Functions Are Generally Unsuitable to Quantify Chirality. *Mol. Phys.* **2005**, *103* (20), 2769–2772. <https://doi.org/10.1080/00268970500217196>.
- (33) Pelayo, J. J.; Whetten, R. L.; Garzón, I. L. Geometric Quantification of Chirality in Ligand-Protected Metal Clusters. *J. Phys. Chem. C* **2015**, *119* (51), 28666–28678. <https://doi.org/10.1021/acs.jpcc.5b10235>.
- (34) Levin, B. D. A.; Jiang, Y.; Padgett, E.; Waldon, S.; Quammen, C.; Harris, C.; Ayachit, U.; Hanwell, M.; Ercius, P.; Muller, D. A.; Hovden, R. Tutorial on the Visualization of Volumetric Data Using Tomviz. *Micros. Today* **2018**, *26* (1), 12–17. [https://doi.org/DOI: 10.1017/S1551929517001213](https://doi.org/DOI:10.1017/S1551929517001213).
- (35) Shaw, L. A.; Chizari, S.; Shusteff, M.; Naghsh-Nilchi, H.; Di Carlo, D.; Hopkins, J. B. Scanning Two-Photon Continuous Flow Lithography for Synthesis of High-Resolution 3D Microparticles: Erratum. *Opt. Express* **2018**, *26* (11), 14718. <https://doi.org/10.1364/oe.26.014718>.
- (36) Chang, Y.-H.; Jang, J.-W.; Chang, Y.-C.; Lee, S.-H.; Siao, T.-F. Gold Nanohelices: A New Synthesis Route, Characterization, and Plasmonic E-Field Enhancement. *ACS Omega* **2020**, *5* (25), 14860–14867. <https://doi.org/10.1021/acsomega.9b02586>.
- (37) Kaschke, J.; Wegener, M. Gold Triple-Helix Mid-Infrared Metamaterial by STED-Inspired Laser Lithography. *Opt. Lett.* **2015**, *40* (17), 3986. <https://doi.org/10.1364/ol.40.003986>.

(38) Yan, J.; Feng, W.; Kim, J.-Y.; Lu, J.; Kumar, P.; Mu, Z.; Wu, X.; Mao, X.; Kotov, N. A. Self-Assembly of Chiral Nanoparticles into Semiconductor Helices with Tunable near-Infrared Optical Activity. *Chem. Mater.* **2020**, *32* (1), 476–488. <https://doi.org/10.1021/acs.chemmater.9b04143>.

Figures

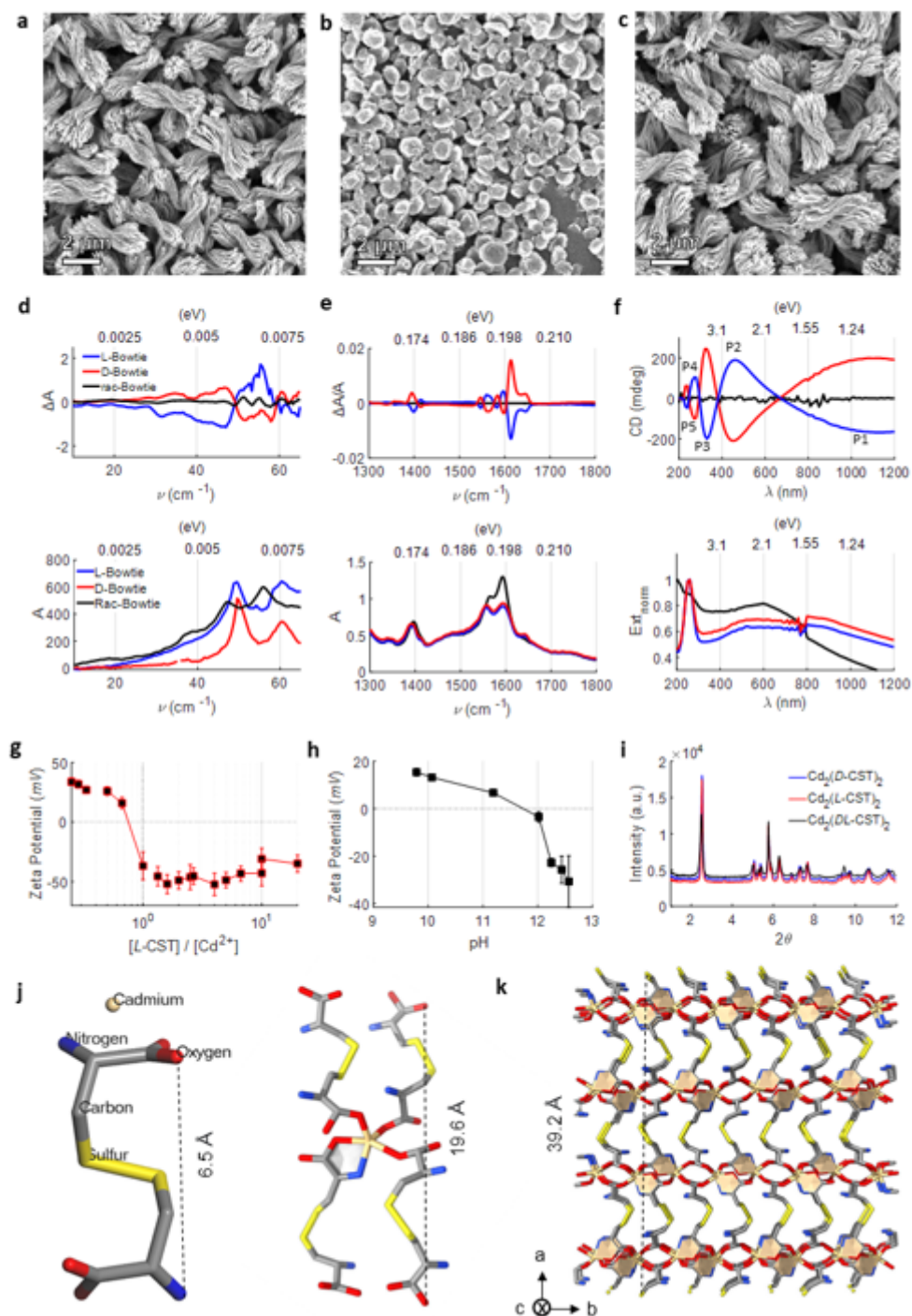


Figure 1

a, SEM images of bowties formed from Cd^{2+} and **a**, *L*-CST (left), **b**, *rac*-CST (middle), and **c**, *D*-CST (right). Scale bars are 2 μm . Circular dichroism (top) and extinction spectra (bottom) in **d**, THz, **e**, mid-IR (VCD) and **f**, UV-vis-NIR ranges for bowtie particles. **g**, Zeta potential of fully formed bowties at different ratios of *L*-CST and Cd^{2+} ions. **h**, Zeta potential of bowties formed from *L*-CST solution at different pH. **i**, Synchrotron XRD pattern and the **j,k**, calculated crystal structure of nanosheets and nanoplatelets forming the bowties. Unit cell is shown in **SI Fig 6**.

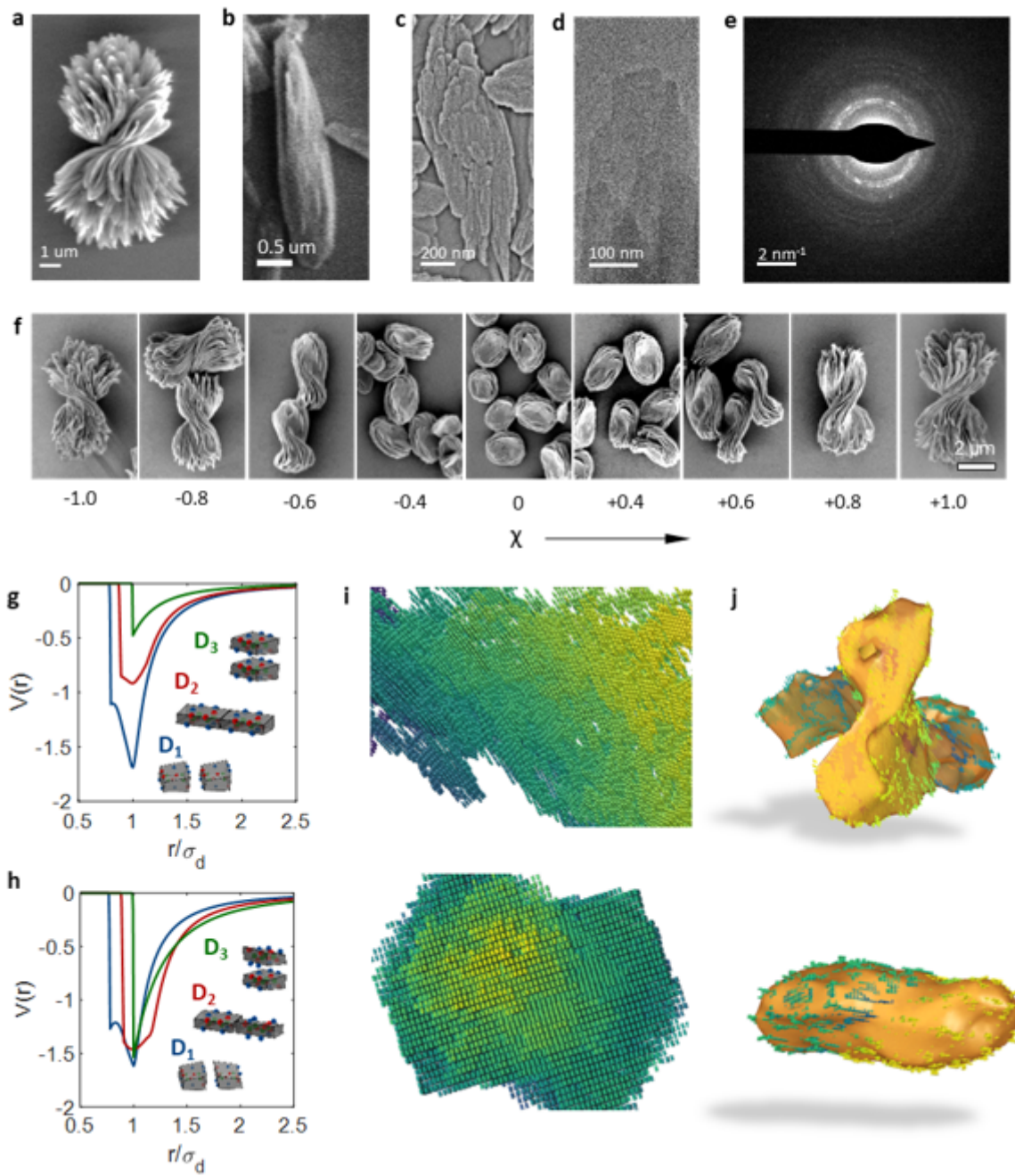


Figure 2

Non-binary evolution of chirality at micrometer scale. **a**, SEM image of a fully formed bowtie, composed of twisted segments that are assembled from nanoribbons (**b**). **c**, SEM image of nanoribbons composed of polydisperse nanoplatelets. **d**, TEM image of the platelet. **e**, cryo-SAED pattern of the nanosheet in **d**. **f**, SEM images of the bowtie particles obtained by mixing different ratios of *L*-CST and *D*-CST, as defined by the enantiomeric excess (χ) show the transition from left-handed to pancake to right-handed bowties. Potentials of mean force obtained for preferred directions of interaction between two basic clusters of two permutations of chirality in CST ligands: **g**, LCL-LCL and **h**, LCD-LCD are computed and used for MC growth simulations. Coarse-grained particle shape deduced from the atomic structure of the nanocluster with the hydrogen bonding interaction sites marked by the spheres in LCL and LCD type nanoclusters are shown. **i**, Magnified snapshots from MC simulations of the fully formed petal shows mismatched domains with local crystalline order arranged to form a (**j-top**) twisted nanoribbon and (**j-bottom**) pancake type petal for LCL and LCD type nanoclusters, respectively. Color coding in panel **i** is for visualization purposes only.

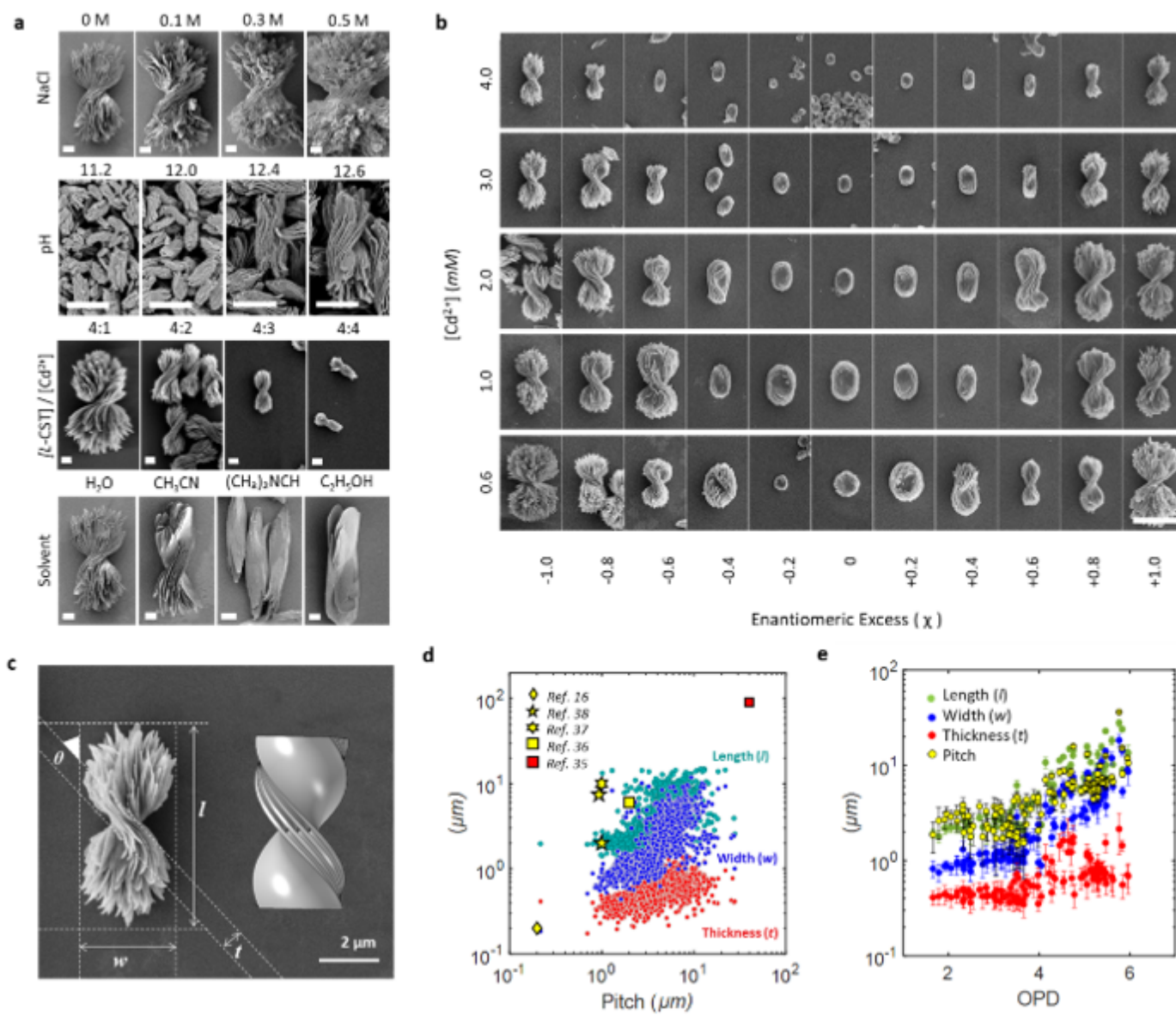


Figure 3

Morphological diversity of bowties. **a**, Effect of NaCl, pH, excess charge (L -CST/Cd), solvent (1:1 water to solvent) on bowtie morphology (water, $[Cd^{2+}] = 1\text{ mM}$, 4 mM for pH, $[L\text{-CST}] = 4\text{ mM}$) are shown. Scale bar in **a** is $1\ \mu\text{m}$. **b**, Continuously variable twist and sizes for bowtie particles obtained for different χ and $[Cd^{2+}]$. Scale bar in **b** is $5\ \mu\text{m}$. **c**, SEM image of a typical bowtie assembly and the corresponding morphological parameters of length (l), width (w), thickness (t) and pitch ($2wtan(90-\theta)$) overlaid. Three-dimensional models (right) used in computations of OPD chirality measures. **d**, Variability of the geometrical parameters for the bowtie assemblies obtained in this study and the same parameters obtained in other studies;^{16,35–38} **e**, Variation of the morphological parameters with OPD chirality measure.

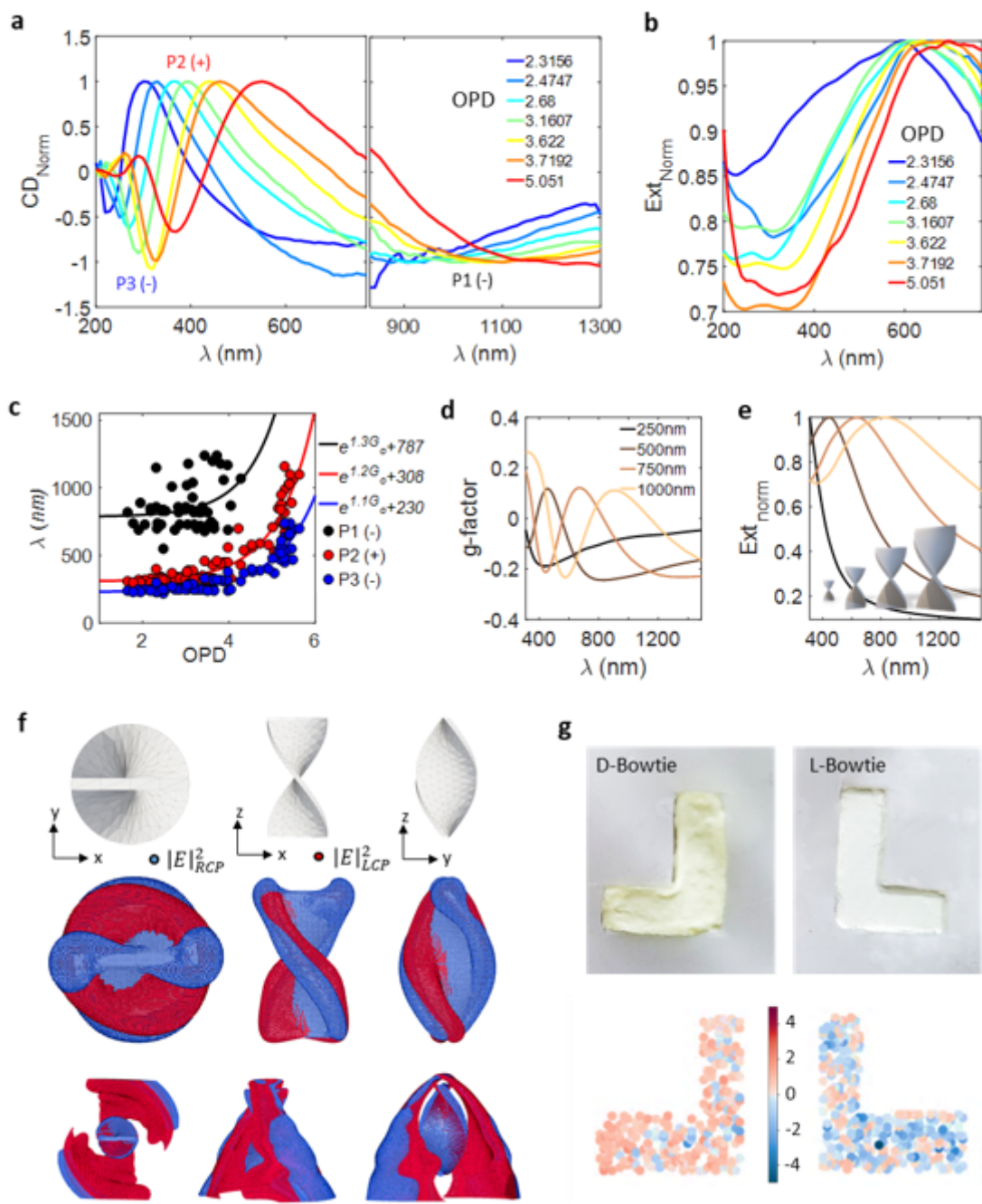


Figure 4

Optical properties of the bowtie particles. **a**, Normalized CD spectra for right-handed bowties of different OPD with peaks P1(-), P2(+), P3 (-) labeled and the **b**, corresponding extinction spectra, **c**, Dependences of spectral position of P1, P2, P3 with OPD made with varying $[L-CST] / [Cd^{2+}]$. For peak P1, the dependence of its position on chirality measures is difficult to assess due to its breadth. **d**, **e**, Calculated g -factor (**d**) and extinction (**e**) spectra are shown here for the twisted ribbon models pictured in the inset with length specified in (**d**). **f**, Projections of 1 μ m long sheet with a left-handed twist used as models for calculation of optical properties. Corresponding electric field maps of $2.5 (V/m)^2$ for scattering resonances for the models interacting with LCP (red) and RCP (blue) of wavelength 1100 nm and 385 nm. The electrical field

around the bowtie model twists stronger when the handedness of photons and the particles is the same. **g**, Photograph of L-shaped coatings printed on glass slides and their images by a 1550 nm LIDAR with circularly polarized detection. No contrast was observed for images based on linearly polarized backscattering.

Supplementary Files

This is a list of supplementary files associated with this preprint. Click to download.

- [SupplementaryInformation1522PK.pdf](#)
- [VideoS1Sliceandviewmovies.mp4](#)
- [VideoS2tomograms.mp4](#)
- [VideoS3onesheetExyHxy.mp4](#)
- [VideoS43Dscatteringfields.mp4](#)